Journal of Renewable and Sustainable Energy
September 2023, Volume 15 Issue 5 Pages 053301 (11p.)
https://doi.org/10.1063/5.0155024
https://archimer.ifremer.fr/doc/00852/96415/

Archimer
https://archimer.ifremer.fr

Blade strain analysis from field measurements on a vertical axis wind turbine

Träsch Martin [1, *], Rosado Hau Nidiana [1], Matoug Camil [2], Arhant Mael [1], Perier Vincent [1], Augier Benoit [1], Répécaud Michel [1]

[1] Ifremer RDT, Research and Technology Development Unit, 1625 route de Sainte-Anne, Plouzané, 29280, France
[2] HydroQuest , 16 Chemin de Malacher, 38240 Meylan, France

* Corresponding author : Martin Träsch, email address : martin.trasch@ifremer.fr

Abstract :

In this paper, the 10 kW WindQuest Vertical Axis Wind Turbine (VAWT) has been instrumented by strain gauges during its trials in the Ifremer in situ test site of Brest to study the effects of the structural dynamic response of the blades under operating conditions. Static and dynamic effects have been investigated as a function of the rotational speed when the rotor operates under stable wind conditions. The analysis segregates the influence of the gravitational, inertial, and aerodynamic loading components on the flapwise bending stress of the blades. The study of the cyclic variations on the blade strain at different Tip-Speed Ratios leads to the identification of the dynamic stall effect on the unsteady loads, while the spectral analysis describes the system eigenfrequencies excited by the interaction of the wind and the structure's motion. The results provide useful data to validate numerical models for VAWT blades with similar design and evaluate the structural fatigue.

Keywords : Wind turbines, Stress-strain analysis, Bending moment, Strain measurement, Aerodynamics, Signal processing, Material fatigue, Strain gauge, Spectral methods, Flow instabilities

Please note that this is an author-produced PDF of an article accepted for publication following peer review. The definitive publisher-authenticated version is available on the publisher Web site.

1. Introduction

The renewable energy technologies play a crucial role towards the world objective of Net Zero greenhouse gas emissions by 2050 [1]. Among the renewable technologies, wind energy has depicted one of the most significant growth in new capacity installed and the reduction in its costs is still forecast for the following years [2, 3]. While the technology of the Horizontal Axis Wind Turbines (HAWTs) presents stable maturity for on-shore applications, the technology for off-shore applications is still under development and efficient structures and installations are needed in order to continue with the reduction in the cost of energy production (COE) [2]. The Vertical Axis Wind Turbines (VAWT) have become of interest in the last few years as a potential floating off-shore structure; some of their attractive characteristics that can promote to off-shore COE reductions are: (i) lower center of gravity and better seakeeping ability that allows easy access for maintenance, (ii) the omnidirectional capabilities which removes an alignment system and (iii) narrower wakes that dissipates faster and reduces the space among the rotors [4]. Therefore, the investigations on VAWTs have increased.

In VAWT devices, while rotating around the vertical axis, the blades experience aerodynamic loads cyclic variations in both the relative wind velocity and the angle of attack impacting the blades [5]. Thus, the estimations of the unsteady loads affecting the blades become a very challenging task in both numerical and experimental approaches [6, 7]. The average power coefficient as a function of the tip speed ratio is the parameter most frequently reported [8]. Furthermore, with the advances in computational fluid dynamic, many in-depth details on the aerodynamics can be obtained, such as the cyclic variations in lift and drag forces while the blade describes a full cycle, the formation of vortices and dynamic stall phenomenon [9, 10, 11, 12].

With the increased interest to install VAWTs under deep-water locations, the development of fast-numerical tools to evaluate both aerodynamic and structural loads is also increasing. Some attempts have been made to propose

aeroelastic numerical models to analyse the dynamic response on the blades of VAWTs. For example, the flutter behaviour on the various VAWT shapes was investigated by using the aeroelastic stability tool OWENS [13] and the local flapwise moment was investigated for different aerofoils by using an aeroleastic code adapted for VAWTs in [14]. A stress analysis on a Troposkein rotor was also performed experimentally and an analytical model was proposed based in the experimental observations in [15]. The blade stress and total deflection were calculated using FEA and beam theory in a helical VAWT [16]. Furthermore, Hand et al. [4] evaluated the bending moment of the blades of a 5MW VAWT when exposed to extreme winds under parked conditions using an analytical model and finite element techniques.

Experimental investigations about the structural dynamics of VAWTs are less common. The SANDIA project dated from the 80's is one of the most complete works considering strain measurements on a Darrieus-type VAWT under parked and rotating conditions [17, 18]. Pagnini et. al. [19] also evaluated the modal frequencies and damping coefficients along the tower of an *in-situ* VAWT from accelerometers measurements. Similarly, the 1HS model [20] was instrumented in its blades, struts, and tower to evaluate the structural loads: flap bending, edge bending, and torsion. Modal analysis on a parked 1kW prototype in wind tunnel with stereo vision has also been reported in [21].

This paper focus in the understanding of the blade deformation behaviour on the blades of a VAWT rotor. The experimental tests were performed under open-field conditions and under the range of rotational speeds where the twin rotor produces positive power. The measurements carried out here with the strain-gauges allow to study the blades deformations behaviour as a function of the azimuthal angle and its spectral components for several values of tip speed ratio. Therefore, it can be considered as an experimental benchmark for VAWTs dynamic blades numerical models validation as well as case load for design and fatigue study.

2. The 10kW WindQuest turbine

The WindQuest design is a counter-rotating Vertical Axis Wind Turbine (VAWT) concept produced by HydroQuest and studied by Ifremer, LEGI and ENSMA research teams. This novel design aims at reducing the Levelised Cost of Energy (LCOE) of Floating Offshore Wind Turbines (FOWT). Indeed, it keeps the advantages of the VAWT technology while seeking to mitigate its disadvantages [22, 23].

The current rotor shape was designed with the aim of reducing the aerodynamic losses and then incorporating the winglet-shaped fixations. As a consequence, this rotor shape increases the power coefficient to values closer to the Horizontal Axis Wind Turbines (HAWT) standards [24]. Moreover, the counter-rotating design was also tuned in order to improve the aerodynamic and seakeeping performance. Previous investigations that have led to this VAWT concept design consist of the numerical study of the counter-rotating VAWT parameters [25], and the experimental investigation of the selected configuration [26, 27].

Experimentation of a 10kW prototype of the WindQuest VAWT design (Fig. 1) is being done as part of a partnership between HydroQuest, GEPS Techno, and the Ifremer. The results presented in this paper were obtained during trials on the prototype installed onshore in the Ifremer *in situ* test station of Brest [28]. Further trials are planned with the wind turbine installed on GEPS Techno's WaveGem floating platform at the SEMREV tests site of Centrale Nantes.

Figure 1: The 10kW WindQuest VAWT in the Ifremer *in situ* test station of Brest

The 10kW WindQuest turbine is a 3.5m-high double rotor O-shaped VAWT. The turbine geometric characteristics are presented in Table 1. The vertical tower is placed between the rotors and links the bearings through two horizontal bars at the top and the bottom of the rotors. The rotors are made to be contra-rotating. However, in this study, only one of them is activated while the other stays still. To counteract for the centrifugal forces, three strut cables are installed between both blades at the positions $0.2H$, $0.5H$ and $0.8H$.

Characteristic	Symbol	Value
Height	H	3.5 m
Rotor radius	R	1.75 m
Blade curvature radius	r	0.35 m
Number of blades	N_b	2
Blade chord	c	0.35 m
Rotor aspect ratio	H/R	2
Blade aspect ratio	H/C	10
Solidity	$N_b c/R$	0.4

Table 1: Geometrical characteristics of the 10kW WindQuest turbine

The blades are built following a NACA0018 profile (see Fig. 2). The blades are made of two 4-mm infused biaxial glass-epoxy composites profiles glued together by a charged epoxy resin. A spar is placed between both profile along the blades, at 1/3 of the chord to stiffen the structure. This spar is made of a square section of two 23mm-thick PVC foam parallelepipeds covered by three 1mm-thick biaxial glass/epoxy layers. An epoxy gelcoat cover has been applied to protect the blade structure from environmental damage.

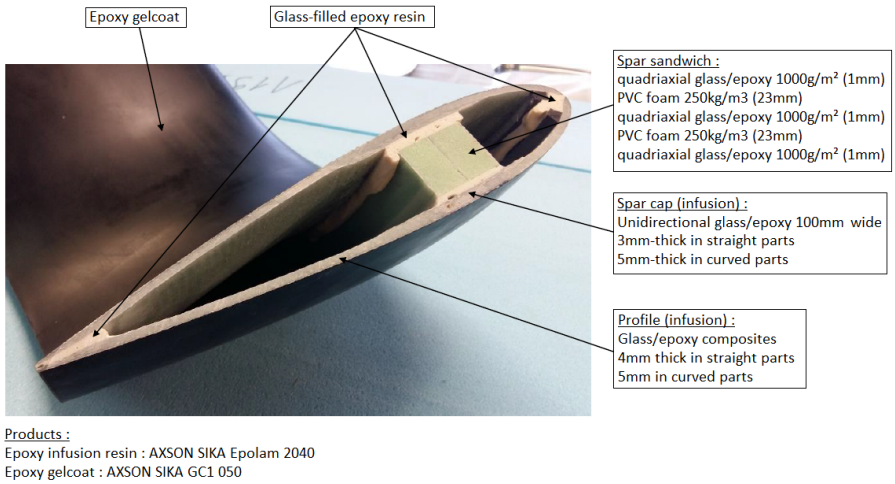

Figure 2: Picture of the blade structure

3. Description of the experiment

Three unidirectional 10/350 LY46-3L-3M strain gauges from HBM are mounted at $1/3^{rd}$ of the chord along one of the blades (Fig. 3) in order to measure the strain in the flapwise direction. They have a resolution of 10μm/m and a sensibility of 1%. The gelcoat layer is removed at the strain gauges position to be directly in contact with the composite skin. They are connected to an autonomous logger that can register the strain data at a sampling frequency up to $f_s = 100$ Hz. The logger is placed directly on the horizontal part of the blade, near the rotation axis to minimize the aerodynamic perturbations. The strain gauges locations are selected to better understand the behaviour of the blade in:

- the position of the strut cable fixation, in the middle of the blade span (gauge n°1).
- the middle of a blade section between two cable fixation (gauge n°2).
- the inside of the curved part of the blade, in what could be the most sensitive part of the blade (gauge n°3).

The strain gauge logger is first calibrated on a glass/epoxy sample in laboratory. To remove the pre-strain component on the signal induced by the gauge installation process, a first reset of the strain signal is then done by the average value measured after the installation of the strain gauges, with the blade resting on the ground, in an horizontal position.

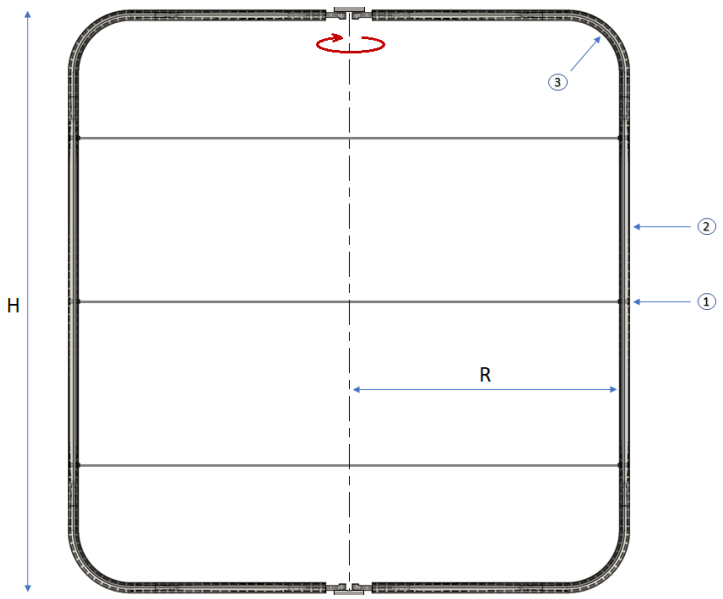

Figure 3: Strain gauges position on one blade of the WindQuest rotor

The wind speed is measured with a LCJ CV7 sonic anemometer placed 5.5 meters high and 37 meters away from the instrumented rotor in the west direction. It gives the two horizontal components of the wind speed with a sampling frequency of 2 Hz.

The rotational speed and the torque are calculated by a Real-Time Model from current and voltage measurements at the output of the electrical generator, which is monitored by Pulse-Width Modulation. In order to characterize the flapwise bending behaviour of the turbine's blades for a wide range of Tip Speed Ratio (TSR), the measurements are carried out under stable wind conditions, and several wind turbine rotation speeds are imposed.

The speed and direction of the wind experienced during the trials are represented in Fig. 4. The wind speed oscillates around $\bar{U}_\infty = 7.1$ m/s in the range of [5.5-9.2] m/s with a south-south-east direction ($\approx 157^o$). For the record, the wind turbines are facing west-south-west (223°). The wind standard deviation during the trials is $\sigma(U_\infty) = 0.65$ m/s. The turbulence intensity is then $I = \frac{\sigma(U_\infty)}{\bar{U}_\infty} = 9.1\%$.

The rotational speed is driven from 50 to 150 rpm, by steps of 10 rpm, with 5 min measurements at each step (see Fig. 4). This rpm range covers the whole rotational speeds experienced by the rotor, and is equivalent to a TSR range from 1.2 to 3.6 (Eq. 1).

$$\lambda = \frac{R\omega}{U_\infty} \tag{1}$$

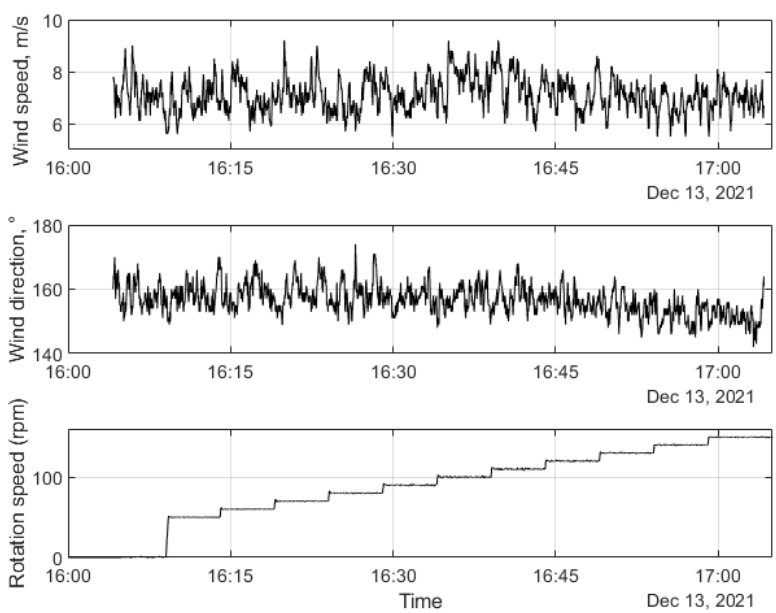

Figure 4: Experimental conditions during the trials

4. Gravitational and Centrifugal loading

The strain results during the trials are presented in Fig. 5. There is an offset of the values at the beginning of the trials, when the rotor is held static and thus, the blades are aligned with the wind. Then, there is a variation of the signal's average and amplitude every 300 s, according to the rotor's rotational speed variations. The initial offset is caused by the reaction of the blade to its own weight, the average variation every 300 s is mainly caused by the centrifugal forces due to the inertia of the rotating blade and the cyclic variations are mostly generated by the aerodynamic forces.

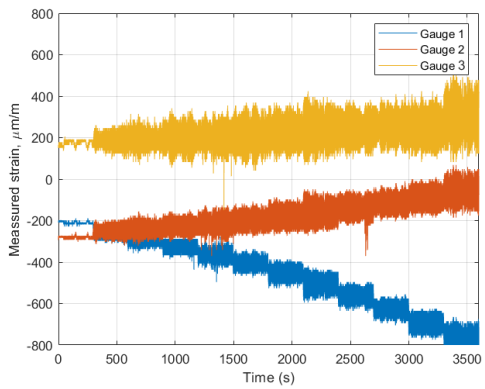

Figure 5: Results of the strain measurements during the trials.

To quantify the influence of these three forces on the strain measurement, a 5 min average of the signals is calculated at the beginning of the records when the rotor is static, and removed from the results. The subtracted values are respectively -208.5 μm/m, -280.1 μm/m and 166.0 μm/m for the gauges 1, 2 and 3. The standard deviation of repeated measurements on a static blade has been found to be always smaller than 17 μm/m.

Averages are calculated using intervals of 180 s for each rotational speed. The results are presented in Fig. 6. First, we can notice that the gauge n°1 measures a negative strain (compression), whereas gauges n°2 and n°3 present a positive strain (extension). Indeed, each blade portion is bent, with on one hand the centrifugal force that pushes it to the outside and on the other hand, the transverse cables that react to this force (see Fig. 7). The results are equivalent to similar measurements in the same prototype obtained during trials under different wind conditions (no wind, more turbulent wind, wind from another direction).

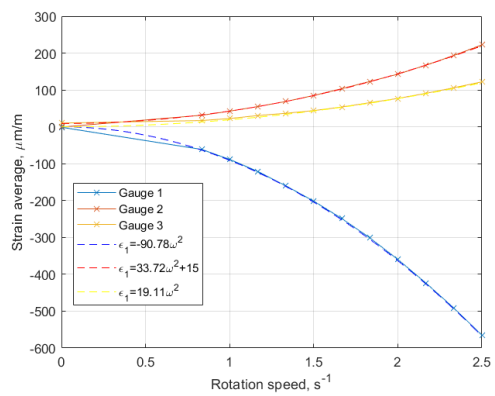

Figure 6: 180 seconds average of the strain results according to the rotor rotation speed and quadratic interpolation

The average strain ϵ_i in each position i evolves with a quadratic behavior according to the rotor's rotation speed ω. A polynomial regression is thus performed on the results (Eq. 2), of which the quadratic coefficients α_i and the norm of the residual are presented in Table 2. $Cste$ is a constant parameter. The high quality of these results is expected as the centrifugal linear load q_c generated by the blade inertia follows Eq. 3, with m the linear mass of the blade and ω the rotation speed in s^{-1} [16].

$$\epsilon_i = \alpha_i \omega^2 + Cste \tag{2}$$

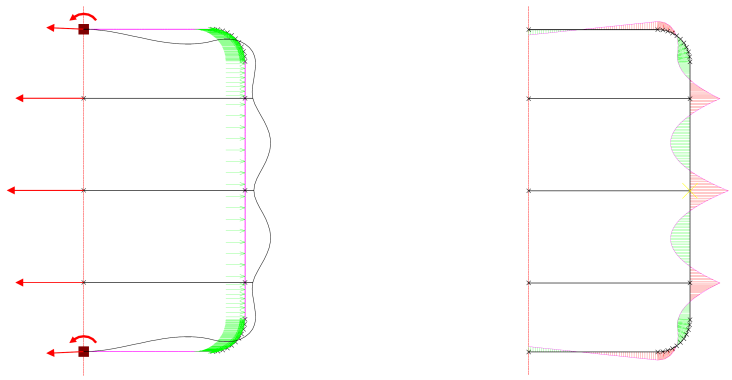

(a) Loading condition and deformation (b) Bending moment

Figure 7: Blade's reaction generated by the centrifugal load as calculated by a RDM7 model.

$$q_c = mR(2\pi\omega)^2 \tag{3}$$

	$\alpha_i(10^{-6}s^{-2})$	R^2
Gauge n°1	-91.51	0.9999
Gauge n°2	30.48	0.9984
Gauge n°3	16.84	0.9899

Table 2: Polynomial coefficients of the average strain fitting in relation to the rotational speed

Assuming that the blade is an homogenous structure with small deflections subjected to lateral loads only, the strain can be estimated by the Euler-Bernouilli linear beam model according to Eq. 4, h being the thickness of the blade, $\mathcal{M}$ the bending moment, E the elastic modulus and I_z the second moment of inertia [16].

$$\epsilon = \frac{\sigma}{E} = \frac{h}{2}\frac{\mathcal{M}}{EI_z} \tag{4}$$

Due to the presence of the transverse cables and the horizontal symmetry of the blade, we can consider the instrumented blade portion to be equivalent to a clamped-clamped beam in order to link the measured strain to the subjected load (see Fig. 7). In this case, the bending moments at the clamped end and at the middle of its length are determined by Eq. 5, where q is the load and L is the length.

$$\mathcal{M}_L = -2\mathcal{M}_{L/2} = -\frac{qL^2}{12} \tag{5}$$

The strain at position 1 and 2 can then be estimated according to Eq. 6. The linear mass of the blade has been measured at $m = 7.26$ kg/m, the second moment of inertia is $I_z = 3.25.10^{-6}$ m^4 and the apparent modulus of elasticity E has been estimated by a four-point flexural test on a blade section to be $E =$ 5.6 GPa. The maximum thickness of the blade is $h = 0.062$ m, the rotor radius $R = 1.75$ m and the considered beam portion is $L = 1$ m. The hypotheses of this analytical model are however not suitable for the estimation of the strain at position 3, which would need a more elaborate numerical model.

$$\epsilon_1 = -2\epsilon_2 = -\frac{\pi^2 mhL^2R}{6EI}\omega^2 \tag{6}$$

This method results in respectively -22% and 17% relative difference with experimental values of α_i (Eq. 2). These differences are considered low enough to confirm that the steady component of the strain is generated by the centrifugal load on the blade. Moreover, this simple analytical model will be used to normalize the cyclic variation of the strain results in the aerodynamic load assessment presented in the following section.

5. Aerodynamic loads assessment

In order to observe the strain variations due to aerodynamic loads, the average values associated to gravity and centrifugal loads are removed. Then, the standard deviation of the strain is presented in Fig. 8 in relation to the Tip-Speed Ratio λ. The cyclic variations of the signals increase with the TSR up to a local maximum at $\lambda = 2.7$, close to the optimal TSR: $\lambda_{opt} = 2.5$. The variations then decrease down to a local minimum around $\lambda \approx 3.3$ before rising again. Their is also a local maximum observed only for gauge n° 3 at $\lambda = 1.7$.

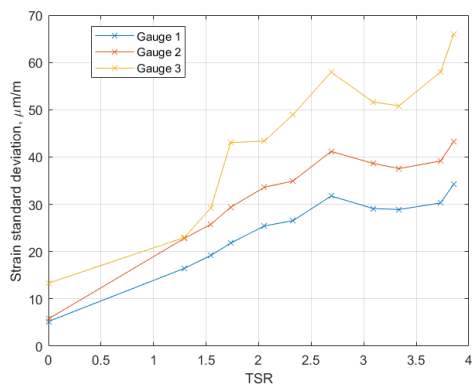

Figure 8: Standard deviation of the strain over 180s-windows for several Tip-Speed Ratios

Phase average of the strain is calculated for a relevant TSR range around the optimal power coefficient ($\lambda \in [1.7-3.5]$). The strain signals are synchronized by detecting the minimum strain for each period of rotation. These minimums are supposed to happen at an azimuthal angle of $\theta = -90^\circ$ (Fig. 9) because in this position the side of the blade is facing the wind, generating maximum radial load towards the rotation centre, and then minimum strain in the gauges positions. That is a strong hypothesis as there could be a shift due to aerodynamic and structural effects induced by the rotation. However, it enables to phase average the results and identify cyclic events. Then, the azimuthal angle is calculated for every points of the rotation period $T = \frac{1}{\omega}$, considering a steady rotation speed.

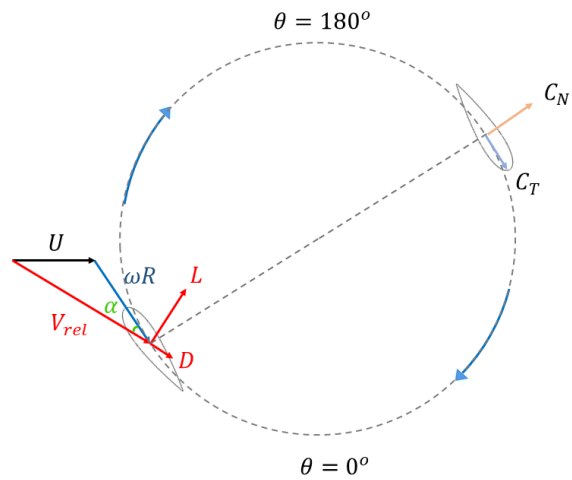

Figure 9: A typical aerodynamic force diagram of a VAWT rotor.

The strain cyclic variations are in phase for every positions. It is an indication that the transverse cables do not act the same way on the dynamic response of the blade to the aerodynamic loads that they do on its static response to the centrifugal load. Therefore, the aerodynamic normal loads assessment is done from the strain variations of the gauge 2 by assuming it is placed on a H-long clamped-clamped beam (Eq. 7). The results of this estimation are presented in Fig. 10. This normal load coefficient should be understood as a "flapwise strain coefficient" representing the level of the blade's flapwise bending. It is useful to compare its order of magnitude and its evolution in relation to other experimental parameters, but it is not accurate enough to be used for quantitative comparison with normal load coefficient obtained through other methods [29, 30].

$$C_N = \frac{q_N}{0.5\rho_{air}cU_\infty^2} = \frac{1}{0.5\rho_{air}cU_\infty^2}\frac{48EI_z}{hH^2}\epsilon_2 \tag{7}$$

In the studied TSR range, the estimated normal load coefficient C_N varies up to $C_N = \pm 10$ during a rotation of the rotor and is close to symmetric. In the literature [31, 30, 16], the normal load variation is higher when the blade is on the upstream side of the rotation ($\theta = 0^\circ$ to 180°). However, the literature focuses on the aerodynamic loads, and not on the dynamic behavior of the blades. This difference is probably due to the inertial response of the blade that generates strain oscillations synchronized with the rotation. The strain then does not reflect directly the loads. That could explain the symmetric behaviour of the hereby calculated normal coefficient, while the aerodynamic loads are higher on the upstream side in the literature. Additionally, the C_N seems higher when the turbine is operating closer to its optimal operating point and is affected by harmonic vibrations, whose importance depends on the rotational speed (higher for $\lambda \approx 2.7$).

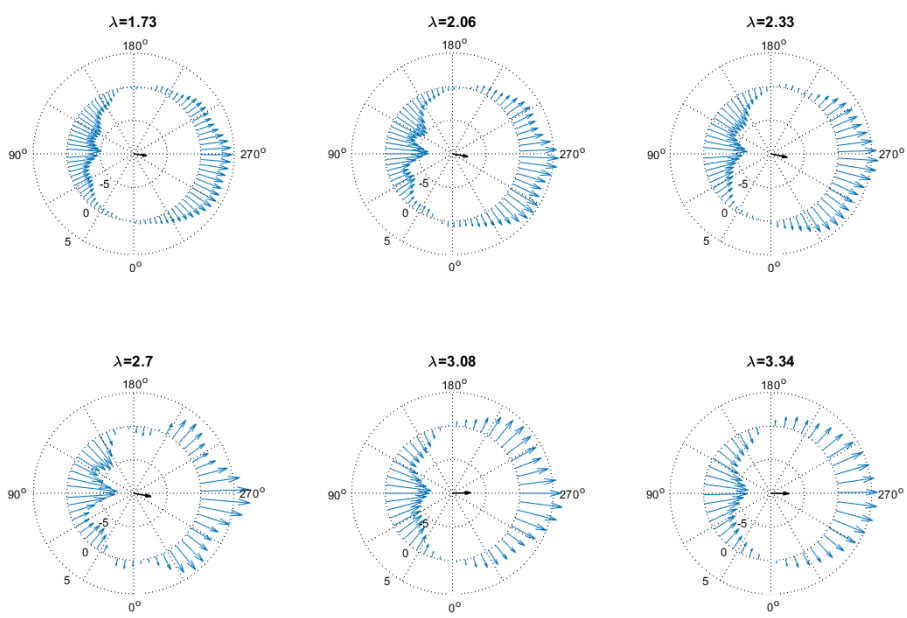

Figure 10: Polar diagram of the blade normal force coefficient. The central arrow is the resultant thrust coefficient.

In order to observe the cyclic behaviour, the same results can be presented considering the apparent angle of attack α and the relative wind speed V_{rel} instead of the wind speed at infinity U_∞. They are calculated by Eq. 8 and 9 [32, 33].

$$\alpha = \arctan\left(\frac{\sin(\theta)}{\lambda + \cos(\theta)}\right) \tag{8}$$

$$V_{rel} = U_\infty \sqrt{1 + 2\lambda\cos\theta + \lambda^2} \tag{9}$$

The normal load coefficient calculated from the relative wind speed $C_N^* = C_N U_\infty^2 / V_{rel}^2$ is presented in Fig. 11 according to the angle of attack α. For $\lambda \geq 3$, the normal load coefficient C_N^* tends to decrease linearly with the angle of attack, with a slope that do change in relation to TSR. Non-linear behavior appears for $\lambda < 3$, where the blade can experience a wider range of angle of attack, that can generate stall (when $\alpha > 20°$), responsible for the hysteresis phenomena visible on the figure 11 [34].

However, the dynamic stall is generally expected to lead to a drop of the load above a given value of the angle of attack. Here, the opposite is observed, with an increase of the load coefficient absolute value. This has already been observed by [35] on an oscillated airfoil for similar reduced frequency $k \approx 0.01$ (Eq. 10). Then, the inertia of the blade could explain why the estimated C_N^* does not go back immediately to its linear behaviour when α returns under pre-stall values.

$$k = \pi\omega c / V_{rel} \tag{10}$$

Results are similar when estimated from strain gauge n°1 using Eq. 7 with a factor 2, with values up to 50% greater that can be due to stress concentration and local structural modification due to the cable fixation. Results from gauge n°3 are also not presented here as they are more perturbed by harmonic vibrations and consequently more difficult to interpret.

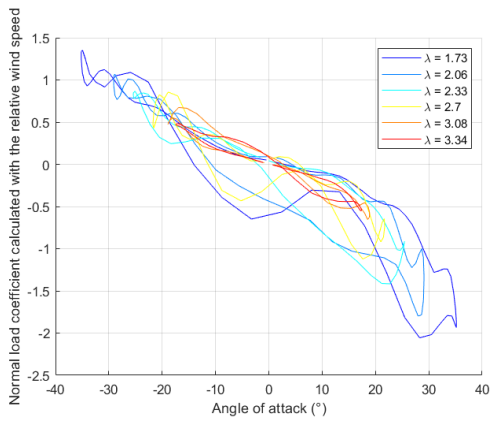

Figure 11: Normal load coefficient estimation from the gauge n°2 calculated with the relative wind speed according to the angle of attack

This load assessment is useful to compare its order of magnitude and its evolution in relation to other experimental parameters, but the normal load coefficient calculated this way is not accurate enough to be used for quantitative evaluation. Therefore, a more elaborate finite elements model would be necessary [4].

The other cyclic variations, especially those leading to harmonic deformations as observed at $\lambda = 2.7$, will be investigated through the spectral analysis presented in the next section.

6. Spectral analysis

The first step of the spectral analysis is to identify the natural frequencies of the system. Therefore, it is done on a portion of strain signal when the rotor is held static, the blades facing the wind. The Power Spectral Densities (PSD) of the strain are calculated on the 4-min signals according to Eq. 11 with $\mathcal{F}$ the Fast Fourier Transform (fft) and N the number of samples. They are presented in Fig. 12. They reveal several peaks at the following frequencies:

- 7.54 Hz, is the frequency of the blade's 1st mode of deformation (Fig. 13a)
- 9.53 Hz is the frequency the blade's 2nd mode of deformation (Fig. 13b). This mode is associated with a more significant deformation in the curved part of the blade when the vertical part is almost not solicited by this mode. It is then only visible in the gauge 3 signal.
- 13.29 Hz, also visible in the signals spectra of the rotating blade. It could be a combination of the first two modes.
- 15.08 Hz, is the first harmonic of the first mode.

$$S_{\epsilon\epsilon}(f) = \frac{1}{f_s N} |\mathcal{F}(\epsilon(t))|^2 \tag{11}$$

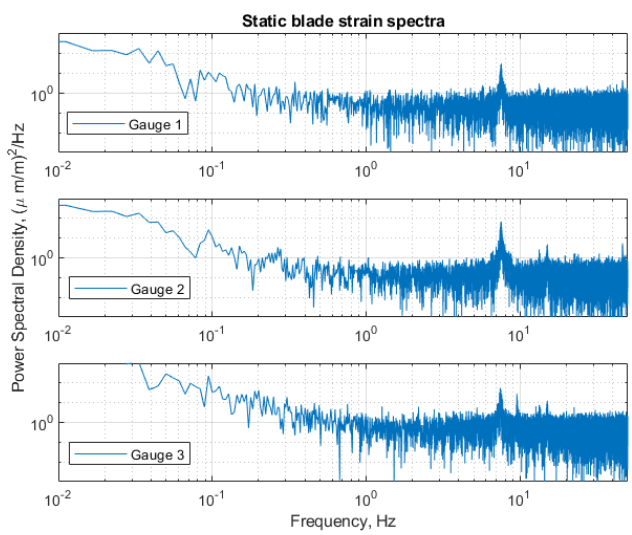

Figure 12: Power Spectral Density of the strain on a log-log scale at the three locations with the rotor held static : rotation speed $\omega = 0$

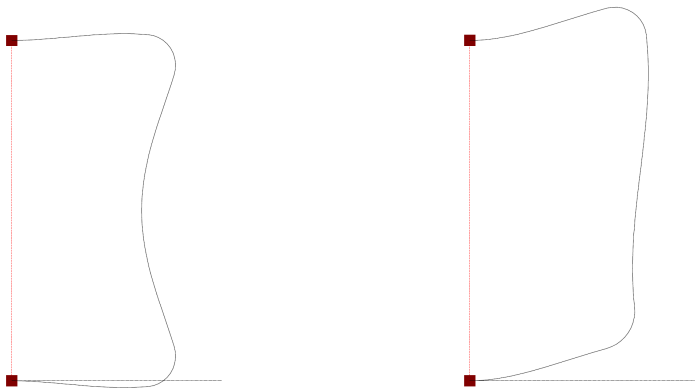

(a) First mode (b) Second mode

Figure 13: Visualisation of the first two deformation modes using RDM 7.

Power Spectral Density of the strain signals when the wind turbine is operating is presented for several rotation speed in Fig. 14. Fig. 14 is a semi-logarithmic graph of the PSD in relation to the frequency f in Hz, whereas the third dimension represents the rotation speed ω. For each signal, peaks are observed at the rotation speed as well as at their multiples, with higher peaks for odd multiples than for even ones.

For every gauges and every tested rotation speeds, peaks at $f = 13.3$ Hz are also observed. It is a natural modal frequency of the system as it has already been observed on the spectrum of the static blade. For the gauge at position n°3, peaks are also observed at $f = 9.5$ Hz, corresponding to the second mode of deformation of the blade (Fig. 13b). However, it seems that the effect of the rotation tends to damp frequencies 7.5 Hz and 15.0 Hz, associated with the first mode of the blade (Fig. 13a).

The perturbations visible in the figure 10 for λ=2.7 (ω = 1.83 Hz) come from the interaction of the rotation speed's odd harmonics with the natural frequencies of the blade, 5ω = 9.2 Hz being close to the second mode natural frequency, while 7ω = 12.8 Hz is close to the 13.5 Hz mixed mode natural frequency. This results in a significantly greater influence of these harmonic vibrations visible in Fig. 10, thus explaining the higher amplitude of the strain observed in Fig. 8 and 11. This resonance phenomenon between natural frequencies of the system and multiples of the rotation frequency also explains the local maximum observed at $\lambda = 1.7$ ($\omega = 1.17$ Hz) for the gauge n°3 in Fig. 8, for which $8\omega = 9.36$ Hz is close to the second mode natural frequency, and the peak for $\lambda = 3.86$ ($\omega = 2.50$ Hz), for which $5\omega = 12.5$ Hz interacts with the first mode natural frequency. The resonance could lead to increased fatigue of the blade structure and material and its hasty deterioration. Therefore, it should be avoided in the wind turbine operation.

In order to verify if this phenomenon also appear when the rotation speed of the turbine is dynamically controled according to the wind speed around the optimal operation point of the turbine, strain gauge measurements were also programmed during normal operation of the VAWT in different wind conditions, with a daily trigger, a sampling frequency of 100 Hz and an acquisition time of 2 minutes. This short time is motivated by the small amount of memory in the logger and the need for high-frequency measurements given the rotor's rotation speed.

These results analysis is complicated by variations in the rotation speed of the wind turbine, that changes according to the command control response to the wind speed, an by the lack of synchronisation with the other measurements of the machine. Furthermore, only some of the recordings are worthy of study, as some of the acquisition windows took place when the wind turbine was at a standstill, while in other cases, there was important signal drift due to temperature changes. The gauges recorded significant cyclic deformations on few acquisitions. The results of three of them are presented in Fig. 15 to 17 with 30-second samples of the signal and the associated spectra.

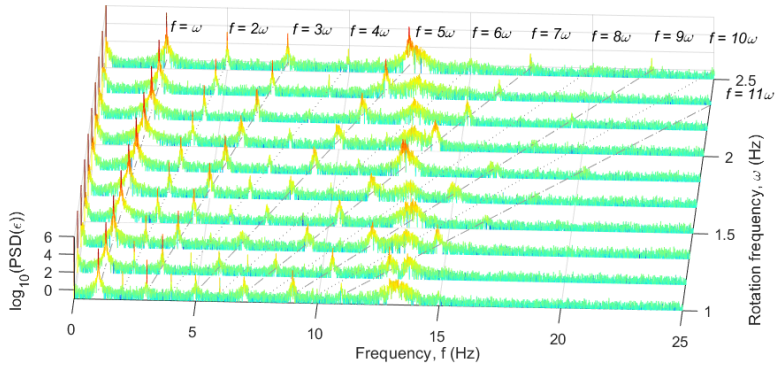

(a) Position 1

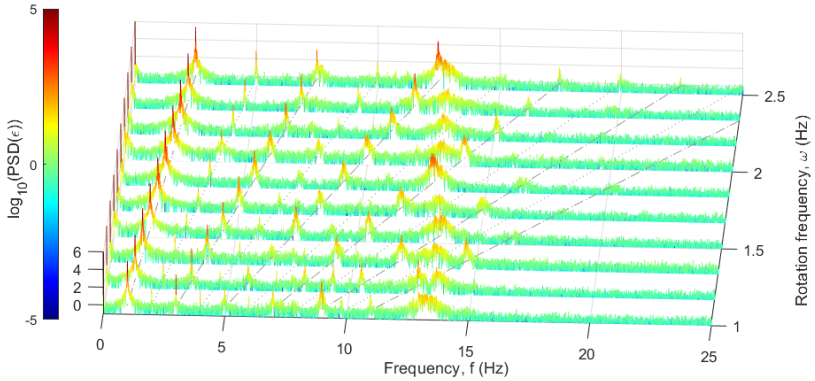

(b) Position 2

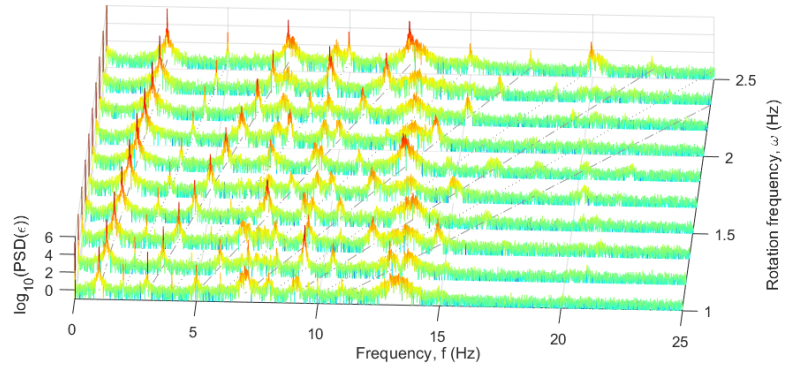

(c) Position 3

Figure 14: Power spectral density of the strain signals for several rotation speed.

Figure 15 shows the deformations when the rotor speed is relatively low and stable, with a rotation of ≈60 rpm. The rotation cycles can be seen on the signal from gauge 1 and a peak close to 1 Hz can be observed on the spectra. In figure 16, the signal corresponds to a rotation that varies between 110 and 150 rpm. The rotation frequency is not clearly visible on the signal, nor on the spectrum, because the signal is too noisy. The spectra show that there is much more energy in the high frequencies. The signal in figure 17 is the one where the maximum amplitude of the deformations occurred, up to 854, 732 and 1502 μm/m respectively for gauges 1, 2 and 5. Here again, the signal is too noisy to see the rotation frequency on the signal or on the spectrum, which must be close to 150 rpm. The spectra show that there is much more energy in the high frequencies.

The average strain of these measurements is consistent with the previous results (see figure 6). However, the natural frequencies previously observed are not visible on the spectra under normal operating conditions. This means that the resonance phenomenon observed at steady rotational speed is significantly lesser or even disappears when the rotational speed is controlled in real time.

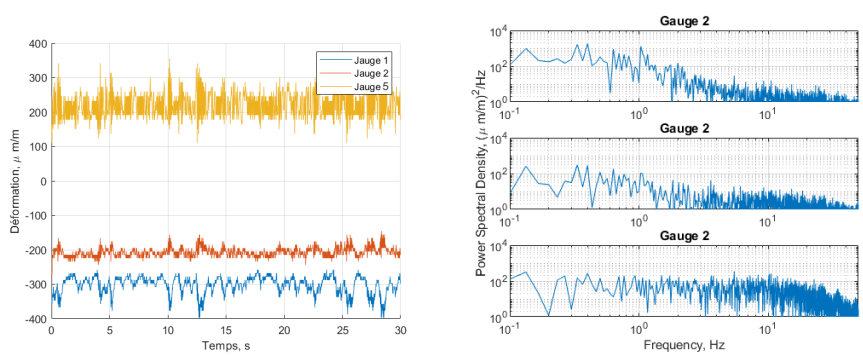

Figure 15: Strain signal (left) and associated power spectral density (right) for a 30s window on normal operation of the wind turbine at a rotation speed around 60 rpm

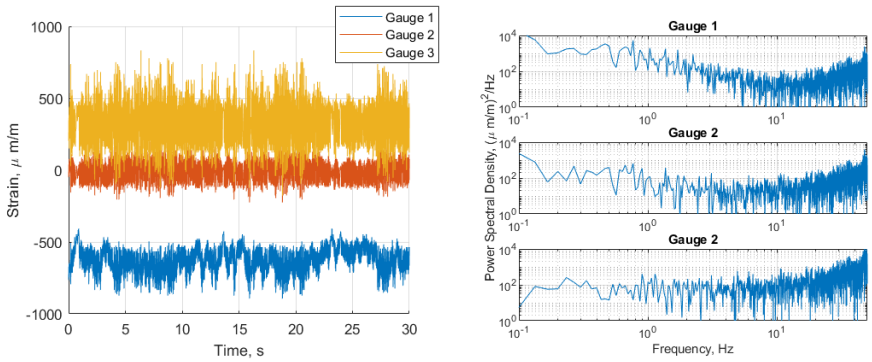

Figure 16: Strain signal (left) and associated power spectral density (right) for a 30s window on normal operation of the wind turbine at a rotation speed around 110 rpm

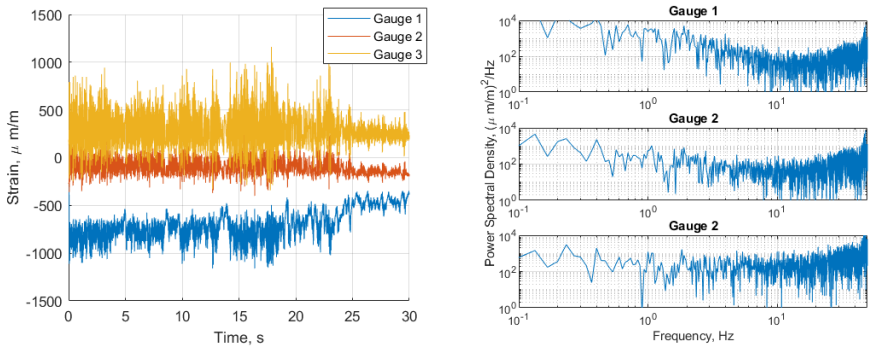

Figure 17: Strain signal (left) and associated power spectral density (right) for a 30s window on normal operation of the wind turbine at a rotation speed around 150 rpm

7. Conclusion

The 10 kW WindQuest Vertical Axis Wind Turbine has been instrumented by strain gauges placed at three different positions on one blade. The flapwise deformation of the blade has then been measured during open field tests with stable wind condition and several turbine rotational speed.

The average deformation is related to the centrifugal loading as confirmed by comparison with a simple analytical model. Cyclic variations of the strain are mostly caused by aerodynamical loading. At low rotation speed, they present a hysteresis behaviour that could be generated by stall at high angle of attack.

Spectral analysis has been used to investigate the harmonic perturbations observed at some specific rotational speeds. It suggested that they occur from resonance between natural frequencies of the system and multiples of the rotation frequency. However, this phenomenon does not seem to occur during the normal operation of the turbine, when the rotation speed is controlled in real time. The author then recommend to avoid operation at steady rotation speeds.

These results will be useful to validate aeroelastic numerical models for VAWTs with similar design [36]. They can also be used in fatigue prediction models to design future vertical axis wind turbine blades. They are to be completed with measurements on the prototype installed on a floating platform in future sea test.

References

[1] L. Joyce, Z. Feng, Global Wind Energy Report 2021, Global Wind Energy Council, 2021.

[2] IRENA, Renewable Power Generation Costs 2020, International Renewable Energy Agency, Abu Dhabi, 2021.

[3] A. Garcia-Teruel, G. Rinaldi, P. R. Thies, L. Johanning, H. Jeffrey, Life cycle assessment of floating offshore wind farms: An evaluation of operation and maintenance, Applied Energy 307 (2 2022). doi:10.1016/j.apenergy.2021.118067.

[4] B. Hand, G. Kelly, A. Cashman, Structural analysis of an offshore vertical axis wind turbine composite blade experiencing an extreme wind load, Marine Structures 75 (2021) 102858. doi:10.1016/j.marstruc.2020.102858.
URL https://linkinghub.elsevier.com/retrieve/pii/S0951833920301519

[5] M. M. Elsakka, D. B. Ingham, L. Ma, M. Pourkashanian, CFD analysis of the angle of attack for a vertical axis wind turbine blade, Energy Conversion and Management 182 (September 2018) (2019) 154–165. doi:10.1016/j.enconman.2018.12.054.
URL https://doi.org/10.1016/j.enconman.2018.12.054

[6] N. Rosado, L. Ma, D. Ingham, A critical analysis of the stall onset in the vertical axis wind turbines, Journal of Wind Engineering and Industrial Aerodynamics 204 (September) (2020) 104264. doi:10.1016/j.jweia.2020.104264.
URL https://doi.org/10.1016/j.jweia.2020.104264

[7] M. T. Nguyen, F. Balduzzi, A. Bianchini, G. Ferrara, A. Goude, Evaluation of the unsteady aerodynamic forces acting on a vertical-axis turbine by means of numerical simulations and open site experiments, Journal of Wind Engineering and Industrial Aerodynamics (2020). doi:10.1016/j.jweia.2020.104093.

[8] A. N. Gonçalves, J. M. Pereira, J. M. Sousa, Passive control of dynamic stall in a h-darrieus vertical axis wind turbine using blade leading-edge protuberances, Applied Energy 324 (2022) 119700. doi:https://doi.org/10.1016/j.apenergy.2022.119700.
URL https://www.sciencedirect.com/science/article/pii/S0306261922009941

[9] Z. Wang, M. Zhuang, Leading-edge serrations for performance improvement on a vertical-axis wind turbine at low tip-speed-ratios, Applied Energy 208 (September) (2017) 1184–1197. doi:10.1016/j.apenergy.2017.09.034.
URL https://doi.org/10.1016/j.apenergy.2017.09.034

[10] C. Li, Y. Xiao, Y. lin Xu, Y. xin Peng, G. Hu, S. Zhu, Optimization of blade pitch in H-rotor vertical axis wind turbines through computational fluid dynamics simulations, Applied Energy 212 (December 2017) (2018) 1107–1125. doi:10.1016/j.apenergy.2017.12.035.
URL https://doi.org/10.1016/j.apenergy.2017.12.035

[11] A. Rezaeiha, I. Kalkman, B. Blocken, Effect of pitch angle on power performance and aerodynamics of a vertical axis wind turbine, Applied Energy 197 (2017) 132–150. doi:10.1016/j.apenergy.2017.03.128.
URL http://dx.doi.org/10.1016/j.apenergy.2017.03.128

[12] W.-H. Chen, C.-Y. Chen, C.-Y. Huang, C.-J. Hwang, Power output analysis and optimization of two straight-bladed vertical-axis wind turbines, Applied Energy 185 (2017) 223–232. doi:10.1016/j.apenergy.2016.10.076.
URL http://www.sciencedirect.com/science/article/pii/S0306261916315197

[13] B. C. Owens, D. T. Griffith, Aeroelastic Stability Investigations for Large-scale Vertical Axis Wind Turbines, Journal of Physics: Conference Series 524 (2014) 012092. doi:10.1088/1742-6596/524/1/012092.
URL https://iopscience.iop.org/article/10.1088/1742-6596/524/1/012092

[14] U. S. Paulsen, H. A. Madsen, J. H. Hattel, I. Baran, P. H. Nielsen, Design Optimization of a 5 MW Floating Offshore Vertical-axis Wind Turbine, Energy Procedia 35 (2013) 22–32. doi:10.1016/j.egypro.2013.07.155.
URL https://linkinghub.elsevier.com/retrieve/pii/S1876610213012411

[15] L. Weingarten, R. Nickell, Nonlinear Stress Analysis of Vertical Axis Wind Turbine Blades, Vol. SAND74-0378, 1975.

[16] P. Marsh, D. Ranmuthugala, I. Penesis, G. Thomas, Numerical simulation of the loading characteristics of straight and helical-bladed vertical axis tidal turbines, Renewable Energy 94 (2016) 418–428. doi:10.1016/j.renene.2016.03.060.
URL https://linkinghub.elsevier.com/retrieve/pii/S0960148116302440

[17] H. M. Dodd, T. D. Ashwill, D. E. Berg, M. E. Ralph, W. A. Stephenson, P. S. Veers, Test results and status of the doe/sandia 34-m vawt test bed (1 1989).
URL https://www.osti.gov/biblio/5491670

[18] Initial structural response measurements for the Sandia 34-meter VAWT test bed, in: ASME, Gas Turbine and Aeroengine Congress and Exposition, 1988.

[19] L. C. Pagnini, G. Piccardo, Modal properties of a vertical axis wind turbine in operating and parked conditions, Engineering Structures 242 (2021) 112587. doi:https://doi.org/10.1016/j.engstruct.2021.112587.
URL https://www.sciencedirect.com/science/article/pii/S0141029621007379

[20] Data Analysis from Experimental Measurements on a Vertical Axis Wind Turbine, Master thesis.

[21] N. Najafi, U. S. Paulsen, Operational modal analysis on a vawt in a large wind tunnel using stereo vision technique, Energy 125 (2017) 405–416. doi:https://doi.org/10.1016/j.energy.2017.02.133.
URL https://www.sciencedirect.com/science/article/pii/S036054421730316X

[22] M. Borg, M. Collu, Frequency-domain characteristics of aerodynamic loads of offshore floating vertical axis wind turbines, Applied Energy 155 (2015) 629–636. doi:10.1016/j.apenergy.2015.06.038.

[23] C. Matoug, B. Augier, B. Paillard, G. Maurice, C. Sicot, S. Barre, An hybrid approach for the comparison of VAWT and HAWT performances for floating offshore wind turbines, Journal of Physics: Conference Series 1618 (3) (2020) 032026. doi:10.1088/1742-6596/1618/3/032026.
URL https://iopscience.iop.org/article/10.1088/1742-6596/1618/3/032026

[24] J.-L. Achard, G. Maurice, G. Balarac, S. Barre, Floating vertical axis wind turbine — OWLWIND project, in: 2017 International Conference on ENERGY and ENVIRONMENT (CIEM), IEEE, Bucharest, 2017, pp. 216–220. doi:10.1109/CIEM.2017.8120794.
URL http://ieeexplore.ieee.org/document/8120794/

[25] M. Guilbot, S. Barre, G. Balarac, C. Bonamy, N. Guillaud, A numerical study of Vertical Axis Wind Turbine performances in twin-rotor configurations, Journal of Physics:

Conference Series 1618 (5) (2020) 052012. doi:10.1088/1742-6596/1618/5/052012.
URL https://iopscience.iop.org/article/10.1088/1742-6596/1618/5/052012

[26] M. Ahmadi-baloutaki, R. Carriveau, D. S.-k. Ting, A wind tunnel study on the aerodynamic interaction of vertical axis wind turbines in array configurations, Renewable Energy 96 (2016) 904–913. doi:10.1016/j.renene.2016.05.060.
URL http://dx.doi.org/10.1016/j.renene.2016.05.060

[27] I. D. Brownstein, M. Kinzel, J. O. Dabiri, Performance enhancement of downstream vertical-axis wind turbines, Journal of Renewable and Sustainable Energy 8 (5) (2016) 0–18. doi:10.1063/1.4964311.
URL http://dx.doi.org/10.1063/1.4964311

[28] M. Träsch, N. Raillard, V. Perier, C. Matoug, M. Le Boulluec, M. Répécaud, Metocean conditions at the ifremer in situ test site in brest, in: Proceedings of the 5th International Conference on Renewable Energies Offshore (RENEW 2018), November 8-10, 2022, Lisbon, Portugal, Advances in Renewable Energies Offshore, Lisbon, Portugal, 2022.

[29] B. LeBlanc, C. Ferreira, Estimation of blade loads for a variable pitch Vertical Axis Wind Turbine with strain gage measurements, Wind Energy (2022) we.2713doi:10.1002/we.2713.
URL https://onlinelibrary.wiley.com/doi/10.1002/we.2713

[30] Q. Li, T. Maeda, Y. Kamada, J. Murata, K. Furukawa, M. Yamamoto, The influence of flow field and aerodynamic forces on a straight-bladed vertical axis wind turbine, Energy 111 (2016) 260–271. doi:10.1016/j.energy.2016.05.129.
URL https://linkinghub.elsevier.com/retrieve/pii/S0360544216307678

[31] E. Dyachuk, M. Rossander, A. Goude, H. Bernhoff, Measurements of the Aerodynamic Normal Forces on a 12-kW Straight-Bladed Vertical Axis Wind Turbine, Energies 8 (8) (2015) 8482–8496. doi:10.3390/en8088482.
URL http://www.mdpi.com/1996-1073/8/8/8482

[32] A.-J. Buchner, J. Soria, D. Honnery, A. J. Smits, Dynamic stall in vertical axis wind turbines: scaling and topological considerations, Journal of Fluid Mechanics 841 (2018) 746–766. doi:10.1017/jfm.2018.112.

[33] A. Laneville, P. Vittecoq, Dynamic Stall: The Case of the Vertical Axis Wind Turbine, Transactions of the ASME 108 (May 1986) (1986) 140–145. doi:10.1115/1.3268081.

[34] W. J. McCroskey, The Phenomenon of Dynamic Stall, Technical Memorandum (TM) 19810011501, Nasa (1981).

[35] K. Tsang, R. So, R. Leung, X. Wang, Dynamic stall behavior from unsteady force measurements, Journal of Fluids and Structures 24 (1) (2008) 129–150. doi:10.1016/j.jfluidstructs.2007.06.007.
URL https://linkinghub.elsevier.com/retrieve/pii/S0889974607001120

[36] N. Rosado-hau, B. Augier, B. Paillard, M. Träsch, C. Matoug, The assessment of a fast computational method in predicting the unsteady loads of vertical axis wind turbines undergoing floating motion, Journal of Wind Engineering and Industrial Aerodynamics 240 (2023). doi:10.1016/j.jweia.2023.105449.